communications earth & environment

Article

https://doi.org/10.1038/s43247-025-02015-8

Two-stage oxidation of petrogenic organic carbon in a rapidly exhuming small mountainous catchment

Check for updates

Wan-Yin Lien[1,6], Chih-Tung Chen[2], Yun-Hsuan Lee[1,3], Chih-Chieh Su[3,4], Pei-Ling Wang[3,4,5,6] ✉ & Li-Hung Lin[1,4,5,6] ✉

Globally, the oxidative flux of petrogenic organic carbon rivals the drawdown by silicate weathering and burial of biospheric carbon. Where and how petrogenic organic carbon is susceptible to degradation along the short-path river-marine continuum in active orogens remains elusive. Here, we demonstrate the transformation of petrogenic organic carbon from a mountainous catchment in eastern Taiwan and its connecting submarine canyon. Our Raman analyses indicate that while highly graphitized carbon in slate/schist transformed into disordered form during soil development, the preferential elimination of disordered form was found along submarine transit. Additionally, quartz/rutile outperformed mica in protecting petrogenic organic carbon from transport abrasion and microbial degradation. Such an oxidative flux was estimated to be 20–35 metric tons of carbon per square kilometer per year, ranking among the greatest levels around the world and highlighting tectonically active islands and the surrounding marine systems as a hotspot of carbon emission.

Erosion and weathering co-regulate carbon transfer between the atmosphere, hydrosphere, and lithosphere through river systems over geological time. Despite extensive studies conducted to characterize the cycling of inorganic carbon through mineral weathering[1–3], petrogenic organic carbon (OC_{petro}) is conventionally treated as a non-degradable entity due to its recalcitrant nature[4], thereby being excluded from the carbon cycle. Recent analyses, however, have started to constrain the bioavailability and the extent to which OC_{petro} is degraded[5–9]. With the approaches such as the isotopic mass balance model or riverine Re proxy, the global oxidation flux of OC_{petro} has been estimated to be 68^{+18}_{-6} MtC yr^{-1}, a quantity comparable with other geological sinks (140 MtC yr^{-1} for silicate weathering and 40–75 MtC yr^{-1} for sedimentary burial of terrestrial biospheric OC)[10–12]. Such a first-order estimate has highlighted the importance of the previously neglected source of CO_2 emission, and the need to unveil the spatial and temporal patterns of OC_{petro} oxidation so that the underlying mechanisms and the global generalized model could be better constrained.

While multiple studies have demonstrated the catchment-scale flux of OC_{petro} oxidation deduced from residual OC contents in sediments or riverine Re proxy, only a few studies offer direct characterization of OC_{petro} alteration using Raman spectroscopy[6,7,13]. These results reveal the presence of highly graphitized OC_{petro} at a higher frequency in downstream river or marine sediments than in upstream river sediments in the Amazon and Himalayan systems, suggesting the differential degradability of OC_{petro} along the river-submarine transit[6,7]. These results also provide profound implications for the preservation of OC prone to hydrodynamic, mineral aggregative, and microbial processes in different compartments across the terrestrial-marine transition.

The oxidation of particulate OC in large river systems occurs mostly during soil development on hillslopes and long-term storage in riparian zones, deltas, and continental margins[14–16]. The prolonged residence time allows for the susceptibility of particulate OC to biogeochemical cycling, leading to the degradation of the recalcitrant organic pool (e.g., OC_{petro}) progressively en route to terminal burial. In contrast, small mountainous rivers with steep topography associated with high exhumation and erosion rates in active margins have been considered to efficiently transfer particulate OC to the deep sea for burial[13,16,17]. While OC_{petro} has been reported to contribute a large fraction to the exported particulate OC in small mountainous rivers in Taiwan, New Zealand, and the Andes (could be up to 70–80%[18–20]; often by definition of zero radiocarbon activity), the negative net CO_2 flux related to OC processes is attributed to the burial of a small quantity of biospheric OC[17]. Furthermore, highly graphitized OC_{petro} from river sediments in Taiwan has been even argued to survive multiple erosion-

[1]Department of Geosciences, National Taiwan University, Taipei, Taiwan. [2]Department of Earth Sciences, National Central University, Taoyuan, Taiwan. [3]Institute of Oceanography, National Taiwan University, Taipei, Taiwan. [4]Science and Technology Research Institute for Decarbonization, National Taiwan University, Taipei, Taiwan. [5]Research Center for Future Earth, National Taiwan University, Taipei, Taiwan. [6]These authors contributed equally: Wan-Yin Lien, Pei-Ling Wang, Li-Hung Lin. ✉e-mail: plwang@ntu.edu.tw; lhlin@ntu.edu.tw

burial-exhumation cycles based on the spectroscopic characterization[13], thereby contributing a negligible impact on CO_2 emission. Nevertheless, this perception could have been challenged by the fact that rapid uplift in active orogens would facilitate the exposure of subsurface unweathered OC_{petro} to enzymatic degradation in surface environments[21]. The inference is supported by the radiocarbon activity of OC with activation energy that spans over a range between those for bedrock and soil end members[5]. However, potential biases could arise due to the fact that OC, subject to various treatments and analyses described above, is attributed to a spectrum of structural and compositional entities. It remains unclear whether the OC_{petro} in small mountainous catchments would have experienced pathways of alteration along the hillslope-river-submarine routing similar to those in large river systems.

This study aims to constrain the fate of OC_{petro} across the terrestrial-marine transition in the context of active orogeny. Raman spectra, and elemental and isotopic abundances of bedrocks, weathered materials, and river and marine sediments distributed over a 240 km transect across the Beinan catchment of eastern Taiwan and its downstream-fed submarine canyon were acquired (Fig. 1). The integrated results offer the direct evidence to determine the transformation and degradability of OC_{petro} and organo-mineral interactions along such a short-path river-marine continuum. Variations in the flux of OC_{petro} oxidation were also assessed using radiocarbon activities of weathered materials associated with different lithologies and were compared with other small mountainous and large river systems with low topographic gradients and broad riparian zones.

Results

A total of 56 samples were analyzed by Raman spectroscopy to retrieve the maturity of OC_{petro}. In brief, a wide range of peak positions and FWHMs (full widths at half maximum) of the G and D1 bands were observed (Fig. 2). For most rock and sediment samples, the center of G and D1 bands spanned from 1580 to 1600 cm^{-1}, and from 1350 to 1360 cm, respectively. The FWHM of G bands ranged between 20 and 60 cm^{-1}, while that of D1 bands was between 30 and 80 cm^{-1}. In contrast, data points for weathered materials and a few bedloads and marine sediments deviated from the spectral pattern described above, with more scattered G (1530–1600 cm^{-1}) and D1 band (1340–1370 cm^{-1}) positions, and broader FWHMs of G (20–100 cm^{-1}) and D1 (30–160 cm^{-1}) bands. The spectral characteristics of OC_{petro} were utilized to derive the total width (the sum of FWHMs of G, D1, and D2 bands) and potential graphitization temperature (Eqs. 2 and 3) to assess the maturity of OC_{petro} (classified into the Disordered, Intermediate Grade, Mildly Graphitized, and Highly Graphitized OC_{petro} in the order of increasing degrees of graphitization). Most rock samples were categorized into the Intermediate Grade (total width ~125 cm^{-1}, calculated temperature ~350 °C) and the Mildly Graphitized level (total width ~90 cm^{-1}, calculated temperature ~450 °C) (Fig. 3a). Only a few exceptions were attributed to the Highly Graphitized level (mostly from the schist in contact with metagranite at DLKW). Most OC_{petro} spectra for bedloads and suspended loads, and half of weathered materials and marine sediments shared similar Raman characteristics and spanned from the Intermediate Grade to the Mildly Graphitized level (Fig. 3b, d, e, f). In contrast, the OC_{petro} for a few bedloads and the other half of weathered materials and marine sediments was characterized by scattered Raman parameters extending towards the Disordered level.

The graphitization-mineral frequency analyses indicated that quartz, rutile, mica, and feldspar in the order of decreasing abundance were the most abundant minerals in contact with OC_{petro} (Fig. 4). For the Mildly Graphitized OC_{petro}, mica was the most abundant mineral in rocks (54%) and weathered materials (48%), while quartz prevailed in bed loads (48%), suspended loads (56%) and marine sediments (50%). For the Intermediate Grade OC_{petro}, quartz dominated in rocks (54%), bedloads (57%), suspended loads (60%), and marine sediments (70%), whereas rutile was prominent in weathered materials (54%) and rocks (32%).

Total organic carbon (TOC) and total nitrogen (TN) concentrations, $\delta^{13}C$, and C/N ratio spanned from 0.07 to 7.65%, from 0.01 to 0.69%, from −28.5‰ to −16.6‰, and from 1.6 to 13.9, respectively (Table S1; Figs. 5 and S1). These wide ranges were mainly derived from bedrocks, weathered materials, and suspended loads. For comparison, narrow-ranging isotopic compositions and concentrations were found for bedloads and marine sediments. Detailed examination further revealed lower $\delta^{13}C$ values of suspended loads than the paired bedloads by 1–4‰ and high variations in TN. The Fm (Fraction modern carbon) values ranged considerably from 0.05 to 0.96 (Fig. 6 and Table S1).

Discussion

Raman spectral characteristics of rock samples

The metamorphic grades of OC_{petro} based on Raman parameters in rock samples were generally in agreement with lithology. Nearly all the OC_{petro} spectral characteristics for slates were assigned to the Intermediate Grade with calculated temperatures spanning from 310 °C to 376 °C, whereas those for most schists were assigned to the Mildly Graphitized level with temperatures ranging from 390 °C to 500 °C (Figs. 3a and S2a). The schist sample in contact with metagranite contained the Mildly to Highly Graphitized OC_{petro}, and had experienced the highest calculated temperature of up to 576 °C. Previous temperature estimates obtained from conventional thin sections by Raman spectroscopy indicate a range between <330 °C and 450 °C for slates and between 450 °C and 500 °C for schists in the Beinan catchment[22]. Additionally, the geothermometer based on carbon isotopic fractionation between graphite and coexisting calcite yielded a similar range of equilibrium temperatures from 320 °C to 460 °C[23]. Notably, temperatures calculated in this study were derived from randomly oriented rock powder rather than thin sections with specific crystalline orientations. While temperature estimates may not be as accurate as conventional methods, the general agreement with estimates from various methods indicates that the Raman spectra collected from randomly oriented particles preserve the source and genesis characteristics. In this regard, the collected spectroscopic data can be further used to address the OC_{petro} oxidation based on spectral transformation in weathered materials and along the fluvial and submarine transit, and to constrain the potential utility in sediment provenance.

The first stage of OC_{petro} oxidation

The Raman characteristics of weathered materials were distributed over a scattered range toward a greater disordered level when compared with rocks (Figs. 3b and S2b). In particular, intensifying degrees of soil development were correlated to decreasing maturities and increasing radiocarbon activities for a suite of samples from the same hillslope (Figs. 3c and S3). Since weathered materials and parental rocks were collected from either the same weathering profile or nearby sites, the difference in Raman characteristics could be attributed to the consequence of in situ processes. Three potential mechanisms might be involved in such spectroscopic transformation, including (1) on-site early diagenesis of non-graphitic OC, (2) entrainment of exogenous OC_{petro}-alike carbon into weathered materials, and (3) in situ degradation of high-maturity OC_{petro}. To address the first mechanism, diagenesis/metamorphism converts biologically derived OC (e.g., plants and algae) into OC_{petro} at >50 °C over geological time scales (e.g., tens of thousands of years)[24]. Such a scenario has been demonstrated with a 5-km thick marine sediment core where extremely disordered OC_{petro} in the upper core was transformed to relatively ordered OC_{petro} at the core bottom extending from Oligocene to Miocene[25]. Considering the geothermal gradient in the Taiwan orogen (29–35 °C km^{-1})[26], the depth required for the conversion would be ~1.5 km below the surface. Additionally, rapid exhumation has proceeded over the last 1 Ma for the studied catchment[27], generating highly dynamic and intense river incision and steep topography. Only limited and temporary deposition of sediments could have occurred in the riverbank and estuary in such a context. As a result, the on-site deposition scenario is ruled out by the lack of thick and stable depositional environments in the region under dynamic tectonic activity. The input of exogenous airborne soot (or so-called black carbon) from anthropogenic activities (e.g., combustion of fossil fuel) and natural wildfires can also contribute to low-maturity Raman spectra[28,29]. The studied catchment is,

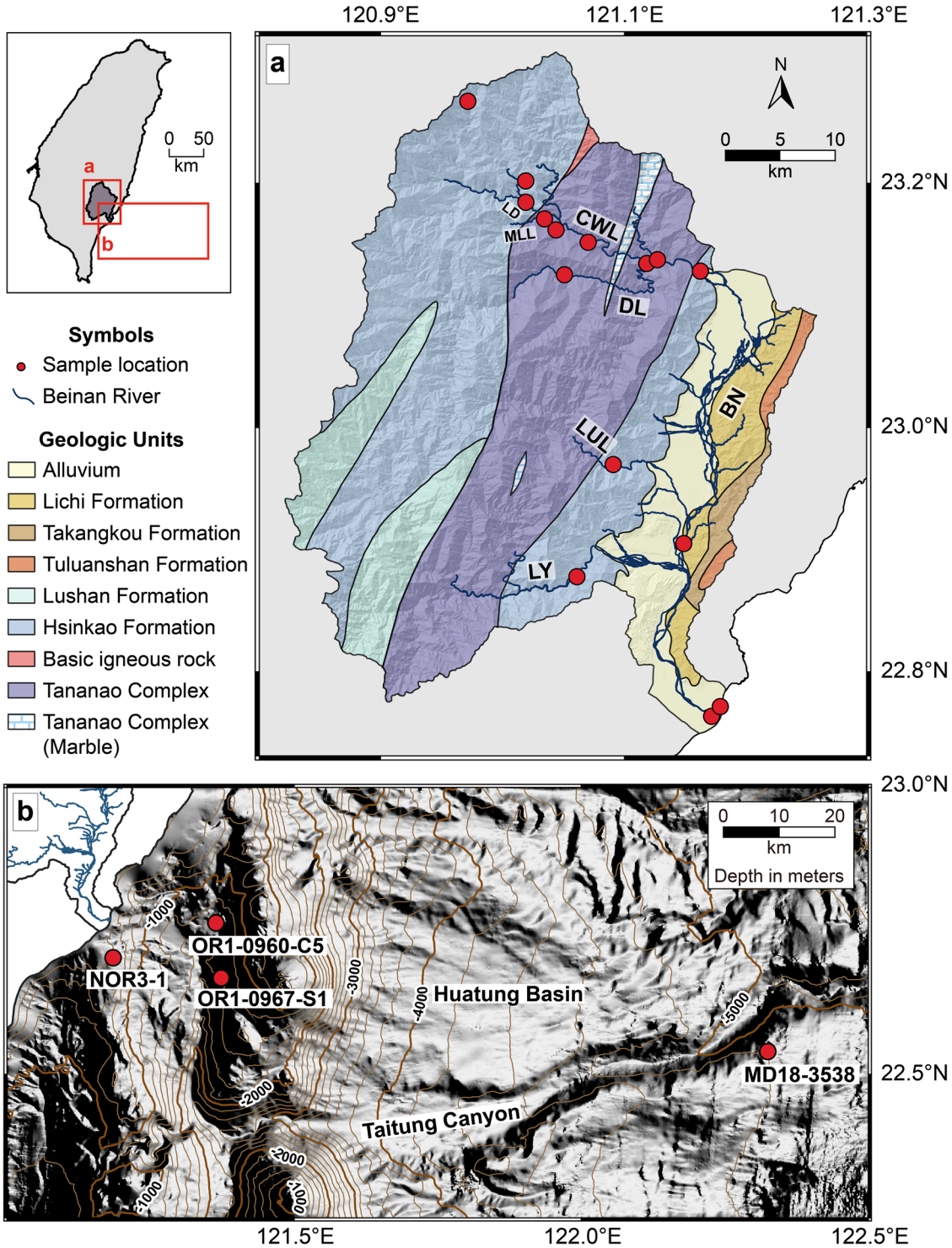

Fig. 1 | Geological and bathymetric maps of investigated regions. a Geological and **b** bathymetric maps of the investigated area are overlaid with the sample sites (red solid circles).

however, distant from the development of infrastructure, industrial manufacturing, and city and only impacted by limited transportation associated with agricultural practice and tourism. Furthermore, airborne soot generally has a size smaller than 1 μm[29]. Considering the size of the analyzed OC_{petro} particles (20–60 μm), the common association between OC_{petro} and minerals, and no plant tissue, it is unlikely to attribute the low-maturity OC_{petro} to exogenous sources through air circulation.

Instead, the transition of OC_{petro} maturity in weathered materials suggests that the origin of the low-maturity OC_{petro} is related to the in situ degradation of bedrocks (Fig. 3b), a pattern analogous to the lab-scale oxidation of highly crystallized graphite over a heating course[30,31] (see Supplementary Discussion 1 for more details). In such cases, biological or enzymatical degradation is involved to lower the activation energy below the threshold that could not be achieved by abiotic processes under ambient conditions[5,32]. Previous studies have demonstrated that OC_{petro} could be directly assimilated into microorganisms[33] and that the degradation of preexisting refractory organic matter in soil could be stimulated by the addition of fresh, labile C and/or N when compared to non-amended

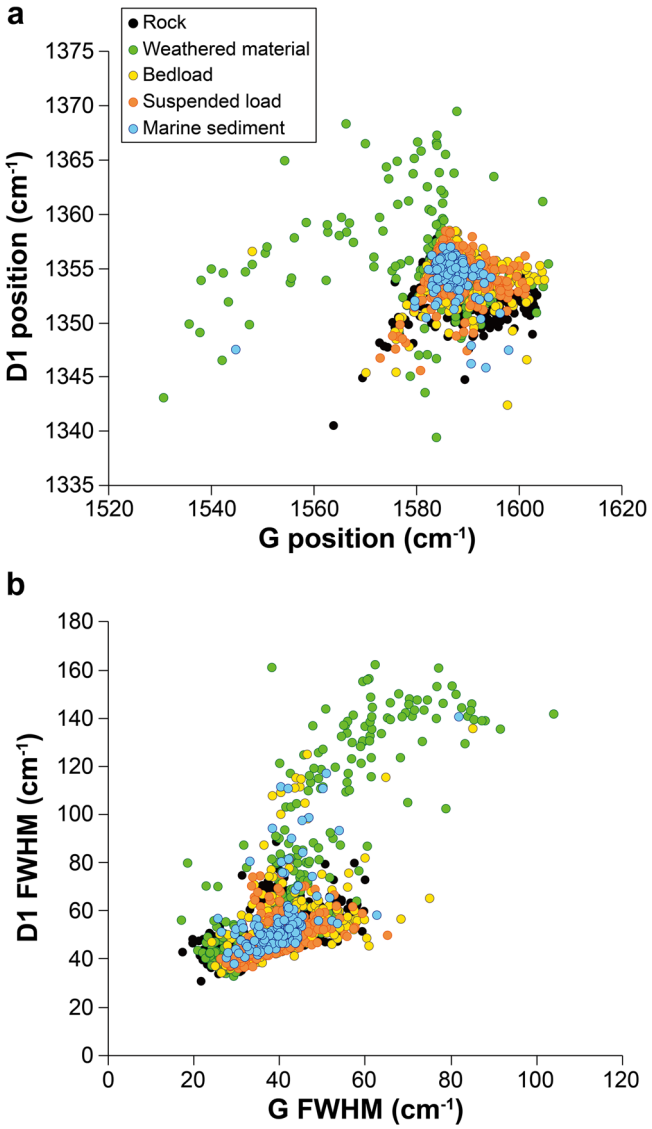

Fig. 2 | Raman spectroscopic characteristics of all analyzed samples. a D1 vs. G band positions (the center wavenumbers for specific Raman peaks). **b** D1 vs. G band FWHMs (full widths at half maximum). FWHM represents an alternative parameter to evaluate the maturity of graphitic carbon (decreases with increasing maturity). Detailed descriptions for acquiring Raman peaks and raw deconvoluted data can be found in Method and Supplementary Data, respectively. Symbol colors: black for rock, green for weathered material, yellow for bedload, orange for suspended load, and blue for marine sediment.

soil[34,35], a process termed as priming effect or co-metabolism. Although the underlying mechanisms are not fully understood, three main types of drivers have been proposed[36], including (1) extracellular enzymes associated with newly introduced fresh organic matter, (2) catabolites from the decomposition of fresh organic matter and plant root exudates for stimulation of successive microbial growth, and (3) organic acids generated by microorganisms and plant roots for disintegration of organo-mineral association. While these drivers are often intermingled and difficult to differentiate from each other, the degradation processes may proceed with the direct decomposition of refractory organic matter by newly introduced exoenzymes. As the reaction advances, catabolites (e.g., sugars, amino acids) and microbial mass build up with the increase in necromass[35], further stimulating microbial and enzymatic activities, which in turn favors the release of refractory organic matter from minerals by leaching with organic acid produced by microorganisms and plant roots[37,38].

The increase in the extent of disordering formed by the in situ biological priming on highly mature graphitic carbon is supported by the inverse correlation between radiocarbon activity and maturity (Figs. 3c and S3). Raman spectroscopy provides the ordering status of graphitic carbon acquired from the peak metamorphism and imposed by potential chemical or biological degradative processes afterward. In contrast, radiocarbon activities represent a mixture of end components of bulk OC (Supplementary Discussion 1). While the spectroscopic difference could be interpreted as the alteration of OC_{petro} during degradation, both the reacted and the resulting graphitic carbon might chemically or isotopically resemble each other with radiocarbon activities equivalent to zero for rocks. Therefore, the increase in radiocarbon activity is best explained by the addition of photosynthetically derived organic matter, whose radiocarbon activity approaches one[5]. In summary, the radiocarbon-free graphitic carbon is likely amalgamated with and spectroscopically modified by newly synthesized organic matter inherited from photosynthesis, thereby cascading the priming effect on the degradative conversion of OC_{petro} into CO_2, and facilitating the net carbon emission from active orogens (Fig. 7).

It is intuitively expected that the priming effect should be pronounced in soil development, through which the weathering front advances with the consumption of bedrocks while newly produced organic matter is additive to the original pool of OC_{petro}[39]. The weathering and priming processes of fresh bedrocks would be limited to the typical downward soil development accompanied by the infiltration of fluids through the pore network and the extension of root systems. Depending on climate conditions, the time scale required to achieve a steady state of soil development might take hundreds of thousands of years[40]. In active orogens, such prolonged progress could be accelerated with rapid uplift and erosion, by which surface soils are removed, and unweathered bedrocks are exposed at a fast pace[21]. Additionally, fractures extending to the depths or pore spaces in pulverized bedrocks derived from tectonic activities offer channels for the transport of oxygen and newly produced organic matter and generate greater areas of reactive surface against the rock pore network[41]. Therefore, the weathering and priming processes could be more prevalent and effective in tectonically active mountainous terranes. Assuming that the weathering profile is in a steady state, the residence time of soils is estimated to range from 20 to 30 yr for 10-cm soils on parental rocks and a denudation rate of 4.5 ± 1 mm yr^{-1} [42,43]. This estimate can be regarded as the lower bound because soils may be mobilized and re-entrained into talus deposits for extended weathering processes. Given the relatively short timeframe, it is more plausible that biological processes play a major role in oxidizing OC_{petro}.

Mechanical mixing of OC_{petro} in river sediments

When compared with all investigated categories, the OC_{petro} in river sediments possessed Raman characteristics distinct from weathered materials and resembling their parental rock materials (Figs. 3d, e and S2c, d). No apparent difference in Raman characteristics was observed between the upstream and downstream sediments or between suspended loads and most bedloads. Furthermore, the maturity range of the OC_{petro} from the weathered bank sediment (#142) and river sediment (#143) in riparian zone was comparable with those from rocks and other river sediments (Figs. S2b, c and S4). The data pattern suggests that the Raman characteristics of river sediments are minimally altered during short-channel transit or retention in riparian zone and represent a mixture of sediments sourced from slate, schist, and rocks with metamorphic grade in-between through erosion, thereby serving as a potential provenance index (see Supplementary Notes 1 and 2 for the estimation of residence time and the provenance index). Although weathered materials develop and are temporarily accumulated on the hillslope, their volumetric contribution to river sediments is apparently negligible as evidenced by the lack of disordered OC_{petro}. Similar inference can be drawn as the $\delta^{13}C$ values and C/N ratios for river sediments clustered in a tighter range when compared with those for bedrocks and weathered materials (Fig. 5). The pattern also suggests a mixture of heterogeneous rock sources for river sediments[44].

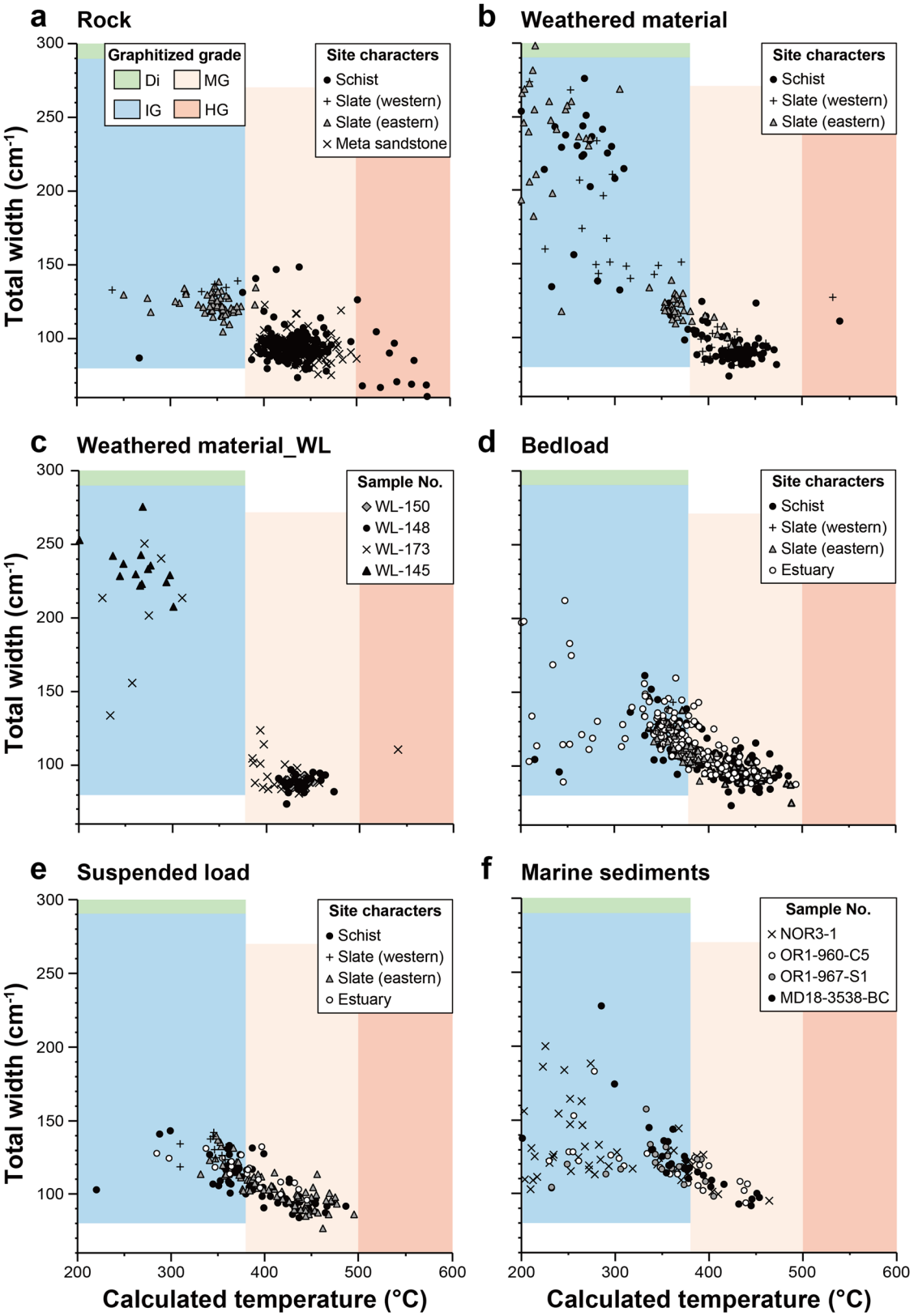

Fig. 3 | Plots of total width vs. calculated temperature for different materials. **a** Rocks, **b** weathered materials, **c** weathered materials with different degrees of weathering, **d** bedloads, **e** suspended loads, and **f** marine sediments. The total width was calculated as the total FWHMs of G, D1, and D2 bands (the ranges of wave-numbers for specific Raman peaks). The calculated temperatures were derived from Eqs. 2 and 3. Di (green), IG (blue), MG (light orange), and HG (orange) in (**a**) stand for the Disordered, Intermediate Grade, Mildly Graphitized, and Highly Graphitized OC_{petro}, respectively, and are the same for the other sub-panels. Symbols: black circle for schist or sample number, plus for slate from the western flank, gray triangle for slate from the eastern flank, cross for meta-sandstone or sample number, white circle for estuary or sample number, gray diamond for sample number, black triangle for sample number, and gray circle for sample number.

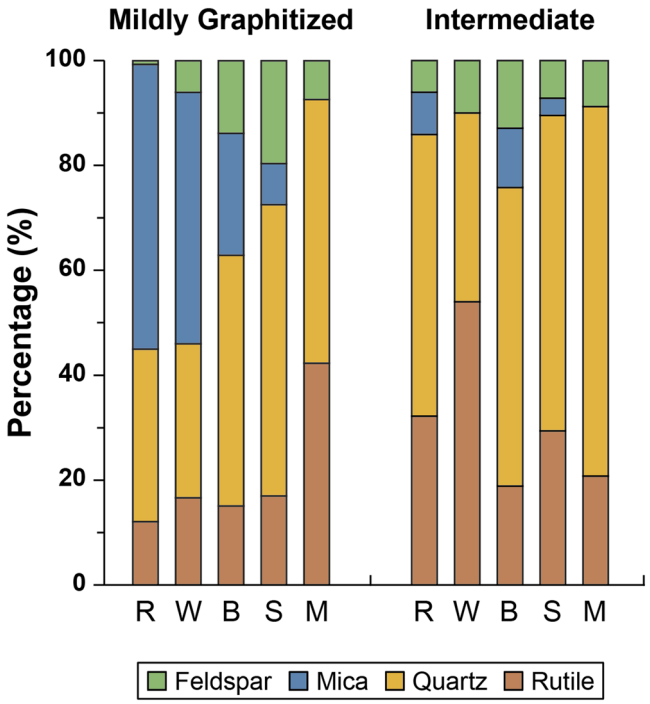

Fig. 4 | Statistic histogram for OC_{petro}-mineral relationships. Abundances of four prevailing minerals (feldspar in green, mica in blue, quartz in yellow, and rutile in brown) associated with OC_{petro} are displayed for different OC_{petro} maturities. Only Raman characteristics with temperature estimates qualified for individual geothermometers were used for statistical analyses. The percentages of the Highly Graphitized and Disordered groups were lower than 1% (out of a total of 1689 spectra). Data for these two groups were excluded from statistics to avoid interpretation bias. R, W, B, S, and M represent rock, weathered material, bedload, suspended load, and marine sediment, respectively.

Data deviating from the general pattern described above were derived from estuarine and sandbar sediments distributed at the outermost boundary between the estuary and shoreline (Fig. S2c, e). The disordered OC_{petro} was found only in sediments collected during the excursion in August 2020. Although OC_{petro} may be susceptible to degradation during prolonged retention at the estuary, the absence of low-maturity OC_{petro} collected at the same locations in other periods of time undermines the possibility of in situ OC_{petro} oxidation. Instead, the data pattern may illustrate the collective nature that sediments in the estuarine outlet and sandbar are sourced from all compartments in the catchment and episodically impacted by erosions induced by torrential waves and river flows during storms or typhoons. Therefore, while the OC_{petro} maturity mostly resembles that in upstream suspended and bedload particulates, the sporadic data off the range defined by the majority suggests the upstream heterogeneity in fluvial processes, sources, and the extent of organic degradation. Finally, a substantial fraction of the disordered OC_{petro} (66%) was recovered from marine sediments near the estuary (Supplementary Discussion 2). This high abundance, coupled with the near absence of disordered OC_{petro} in river sediments, suggests that weathered materials tend to bypass fluvial systems and temporarily deposit in the estuary (Fig. 7).

The second stage of OC_{petro} oxidation

Our analyses reveal that farther marine surface sediments contained a higher percentage of high-maturity OC_{petro} than nearshore sediments (Fig. 3f). To address this, the sedimentological context is first assessed. The sedimentary facies of the Taitung Canyon are characterized by frequent channelized turbidity currents[45,46]. Considering the relative coarse size of analyzed particles (20–60 μm) retrieved from the levee adjacent to the canyon channel, the obtained spectral and compositional signatures represent the event-triggered turbiditic flow overflowing the canyon. Two potential mechanisms are proposed to account for the seaward increase in OC_{petro} maturity, including hydrodynamic sorting[47] and preferential degradation[6,7]. Hydrodynamic sorting is determined by fluid regimes and physical properties of sediments (i.e., particle size and density). Since all the targeted particles are derived from fluidized and poorly sorted turbidite and have similar grain size and density (1.9–2.2 g cm^{-3})[48], the nearshore OC_{petro} signatures would be carried over to distal marine sediments, generating a relatively homogeneous distribution of OC_{petro} maturity along the channel transport. However, the outcome is inconsistent with our observation. Furthermore, low-maturity OC_{petro} may have a lower density than its high-maturity counterpart due to the presence of microporous textures and volume expansion[49,50]. This would have led to a greater distance of transport for low-maturity OC_{petro}, which is again contradictory to our observations. In summary, no apparent driver related to hydrodynamic sorting could selectively partition high-maturity OC_{petro} to the deep sea from low-maturity OC_{petro} around the river outlet.

Alternatively, the data pattern can be attributed to the preferential degradation of low-maturity OC_{petro} with the preservation of high-maturity characteristics (Fig. 7). The rationale stems from the inference that low-maturity OC_{petro} with more impurities and defects is more chemically and biologically reactive than well-crystallized OC_{petro}[51,52] (Supplementary Discussion 1). During long-distance transport, offshore marine sediments entrained by turbidity currents are subject to multiple cycles of settling and resuspension, hence prolonging oxygen exposure[48,53]. This can lead to the enhancement of degradation for low-maturity OC_{petro} prior to its ultimate deposition. Such selective degradation has also been observed in the distal Bengal Fan and downstream Amazon tributaries, where less mature OC_{petro} has almost disappeared with concomitant preservation of high-maturity form over a course of more than 1500 km[6,7]. For comparison, the transport distance for this catchment from the estuary to the most distal site is ~160 km. The residence time of the upper 1-cm surface sediments in Huatung Basin is estimated to range from 10 to 30 yr considering the hemipelagic sedimentation rate (0.3–1.1 mm yr^{-1})[54]. The preferential oxidation of less mature OC_{petro} by microbial processes appears to be feasible even for the short transport distance and residence time across the small island catchment and distal marine depocenter at a scale of hundreds of kilometers within decades.

Mineral association

Mineral abundances of rocks and weathered materials in the Mildly Graphitized group were comparable (Fig. 4). In comparison, the abundances of rutile and quartz were greater and less in weathered materials than in rocks in the Intermediate Grade group, respectively. Since the rock represents the sample category with the least extent of degradation, the pattern suggests that the Mildly Graphitized OC_{petro} is recalcitrant to biodegradation under ambient conditions regardless of the associated mineral. In contrast, the selectivity of mineral protection becomes prominent for the Intermediate Grade group. The high abundance of rutile suggests a specific occurrence related to the preservation of OC_{petro} likely due to its weathering-resistant nature[55].

Along the transit from rock to marine environments, the abundance of mica declined markedly and completely diminished in marine sediments (Fig. 4). In comparison, the abundances of rutile and quartz increased, and those of feldspar were comparable between different sample types. The results reveal a strong dissociation of mica-OC_{petro} relationship during sediment transport. The pattern is inconsistent with the dissolution rate determined from theoretical calculations with experimental constraints through which plagioclase dissolves at a rate about one, or even up to three[56], order(s) of magnitude greater than that of the mica group (e.g., muscovite and phlogopite)[57]. Even considering that feldspar may be falsely identified as laumontite (zeolite group) with similar spectral characteristics, their dissolution rates are comparable to each other[58]. The chemical weathering processes cannot account for the observed patterns of mineralogical abundances across different compartments. Instead, the selective

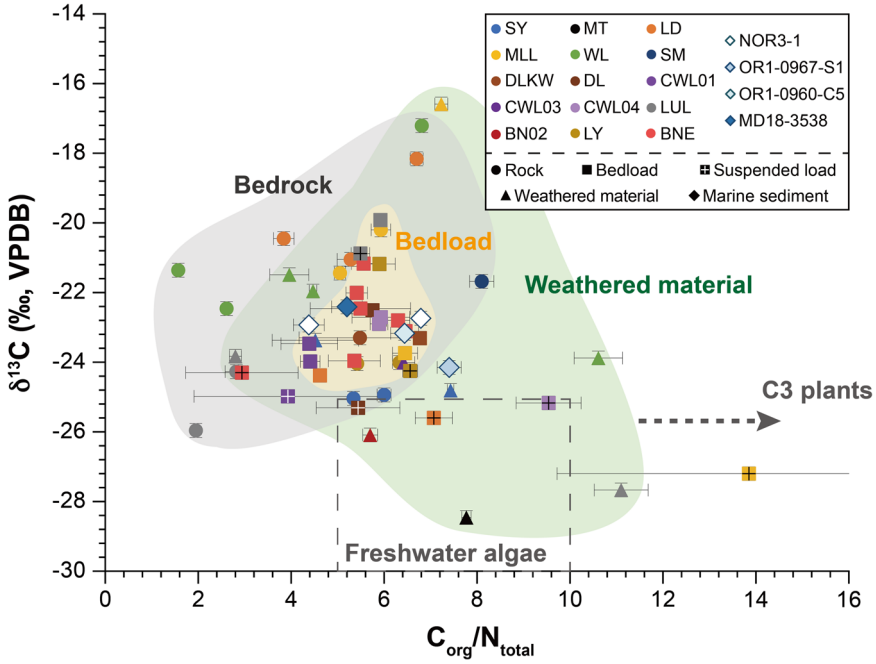

Fig. 5 | Plot of $\delta^{13}C$ vs. C/N ratio with respect to sample location and type. Shaded areas represent the data ranges for three major sample types (bedrock in black, weathered material in green, and bedload in yellow). All error bars are shown as ±1σ (details in Table S1). Typical ranges for biospheric OC, including C3 plants and freshwater algae, are shown using a dashed arrow and a dashed rectangle, respectively[84]. Symbols: circle for rock, square for bedload, square with a plus for suspended load, triangle for weathered material, diamond for marine sediment. Symbol colors correspond to sample locations as indicated in the legend.

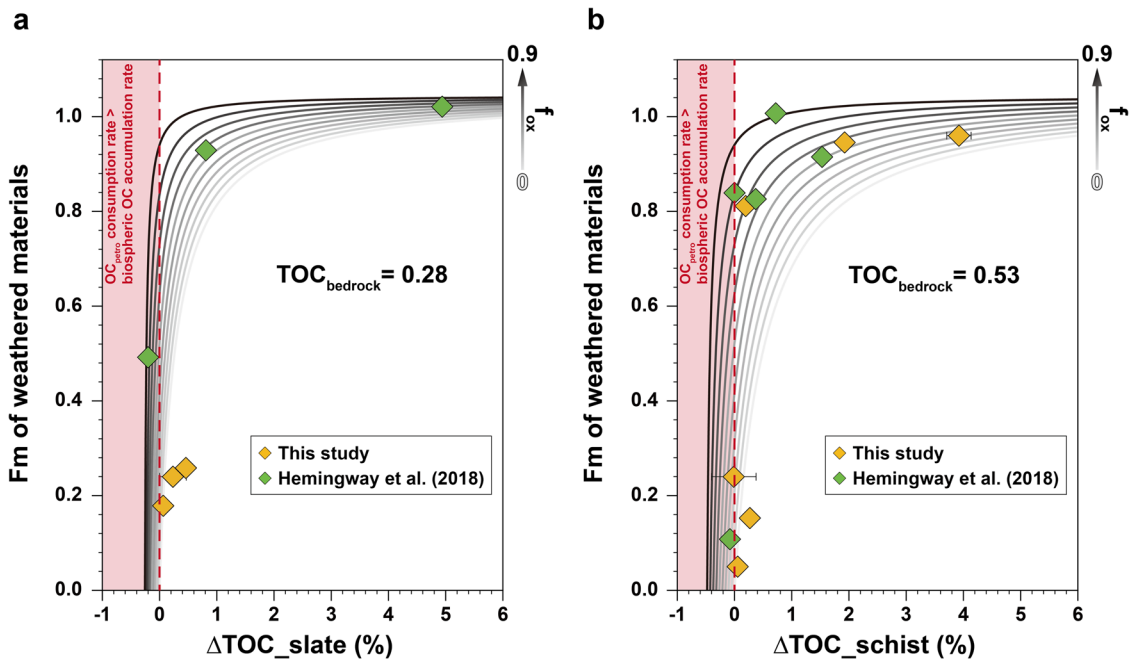

Fig. 6 | Plots of Fm vs. ΔTOC for slate and schist. The curves that represent the relationship between Fm and ΔTOC are projected using Eq. 1, assuming constant $TOC_{bedrock}$ (average values obtained in this study) of 0.28% for slate **a** and 0.53% for schist **b**. Curves with different scales of gray represent the variation in f_{ox} (0 for the lightest gray and 0.9 for the darkest gray). For any individual sample, the curve pattern varies with its corresponding $TOC_{bedrock}$. The data obtained from this study (yellow diamonds) and the previous study for only the samples from the Beinan catchment (green diamonds[5]) are overlaid to constrain the possible range of f_{ox} values. The parental lithology for weathered material at BN02 is uncertain. Therefore, its data are shown in both figures using the average upstream $TOC_{bedrock}$ of slate and schist. The dashed line highlights the zero net OC accumulation rate. Data points yielding negative f_{ox} or in shaded areas (OC_{petro} consumption rate > biospheric OC accumulation rate) are beyond reality, and therefore excluded from the f_{ox} estimation. All error bars are shown as ±1σ. Fm: Fraction modern carbon; ΔTOC: the difference of TOC concentration between weathered material and its parental bedrock ($TOC_{bedrock}$); f_{ox}: the oxidation fraction of OC_{petro}.

elimination of mica may result from the vulnerability of the platy structure, which is susceptible to physical abrasion and grinding associated with sediment transport across the river and marine environments.

The distribution pattern of mineral-OC association is, however, inconsistent with previous studies which reveal efficient protection by expandable phyllosilicates through intercalation into interlayers and by Al-Fe oxyhydroxides through ligand exchange[59]. In addition to the potential interference of spectral acquisition (Method), this discrepancy might arise from short-channel transit and rapid deposition in tectonically active regions, which prevents OC from integrating into mineral structures. Additionally, the association between OC_{petro} and minerals may originate from parent rocks. Over a source-to-sink path, durable and

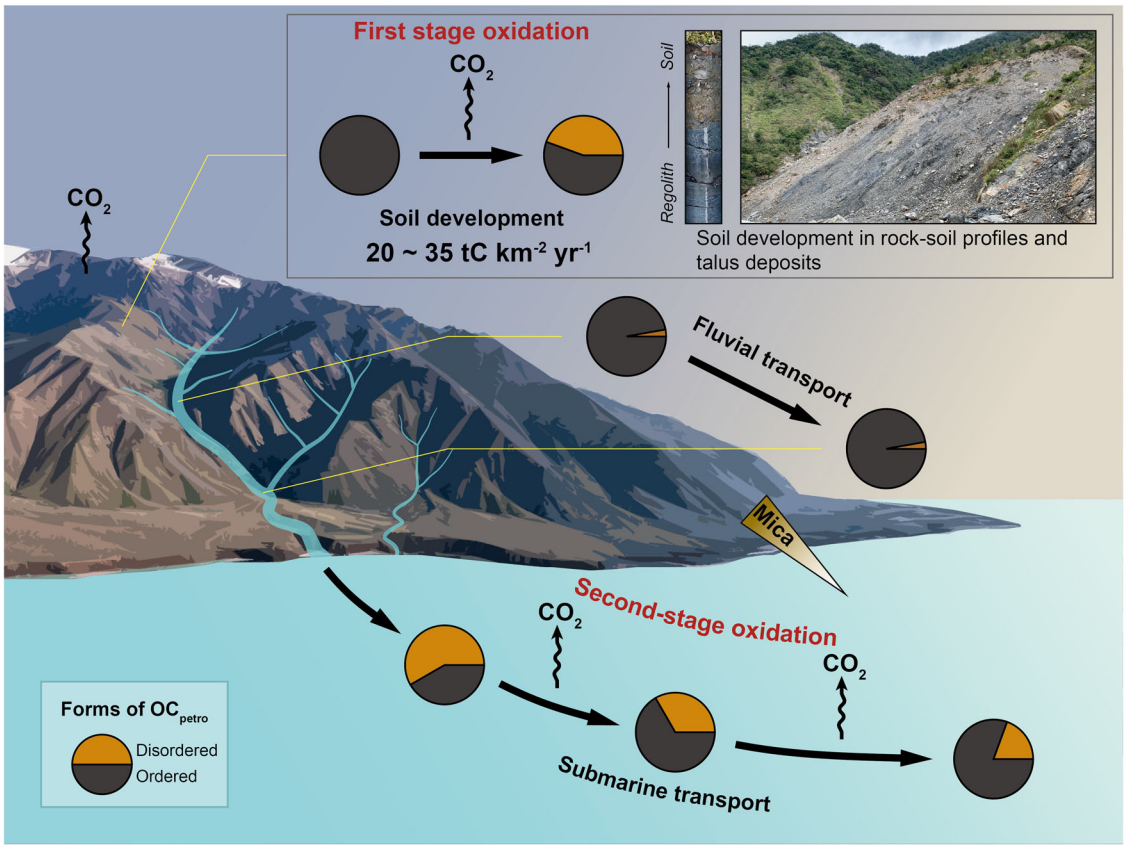

Fig. 7 | Schematic diagram of two-stage oxidation of OC_{petro}. The pie charts depict the schematic proportions of disordered (orange) vs. ordered (gray) OC_{petro}. The oxidation proceeds with transforming highly mature OC_{petro} into disordered form with concomitant CO_2 production (20–35 tC km^{-2} yr^{-1}) in rock-soil profiles and talus deposits during soil development. The resulting OC_{petro} with a spectrum of maturity is eroded and entrained into river systems, and experiences limited microbial degradation. The second stage of OC_{petro} oxidation occurs during submarine transport by degrading more disordered OC_{petro}, thereby enhancing the preservation of highly mature OC_{petro} in the distal abyssal plain. Across the river and marine realms, mica underperforms quartz/rutile in protecting OC_{petro} from physical abrasion and pulverization.

weathering-resistant minerals (e.g., rutile and quartz) provide more direct and effective shielding of OC_{petro} against degradation and transport-associated abrasion and pulverization, leading to the enhanced proportions of specific minerals bounded with OC_{petro} in downstream and distal sediments. In contrast, minerals such as mica would be successively eliminated by physical abrasion (Fig. 7), which subsequently increased the contact area between OC_{petro} and water/air. The weathering would be more intense, resulting in more extensive degradation of recalcitrant OC_{petro}.

Implications for carbon cycle

To estimate the CO_2 flux corresponding to OC_{petro} remineralization on land, the oxidation fraction of OC_{petro} is first evaluated based on the following equation[5]:

$$Fm_{wm} = Fm_{bio}\left[\frac{\Delta TOC + f_{ox}\cdot TOC_{bedrock}}{\Delta TOC + TOC_{bedrock}}\right] \quad (1)$$

where Fm_{wm} is the measured radiocarbon activity of weathered materials and represents the mixture of two end members, biospheric ($Fm_{bio} = 1.045 \pm 0.079$)[5] and bedrock ($Fm = 0$) components, ΔTOC is the difference of TOC concentration between weathered material and its parental bedrock ($TOC_{bedrock}$), and f_{ox} is the oxidation fraction of OC_{petro} between 0 (no remineralization) and 1 (complete remineralization). The calculation predicts the variation in Fm_{wm} between one end represented by a high input of biospheric OC into weathering products (resulting in a Fm_{wm} value of approximately 1 and a high ΔTOC), and the other end represented by zero accumulation of biospheric OC (Fig. 6). Although orthogonal distance regression has been used to simultaneously approximate the best-fit f_{ox} and $TOC_{bedrock}$ [5], the fitting results are reliable only when the OC_{petro} from different profiles are degraded at the same pace. The approach might be applicable to sedimentary terranes but appears to be unrealistic for active orogens with heterogeneous lithology, steep topography, and dynamic climate. As revealed in this and previous studies[44], bedrock composition alone can exhibit a wide variation. Therefore, the modeling for f_{ox} was performed on individual samples using their corresponding $TOC_{bedrock}$. The resultant f_{ox} values were further categorized in accordance with lithology and averaged to yield 0.65 ± 0.12 for slate and 0.49 ± 0.29 for schist distributed in the catchment (Fig. 6). The correlation between Raman data and f_{ox} is further discussed in Supplementary Note 3.

Based on the average $TOC_{bedrock}$ and f_{ox} of each rock type, the OC_{petro}-derived CO_2 emission fluxes from slates and schists were calculated to be 23 ± 7 tC km^{-2} yr^{-1} and 33 ± 21 tC km^{-2} yr^{-1}, respectively (see detailed calculation in Supplementary Note 4). If the variation in $TOC_{bedrock}$ is taken into account, the oxidation flux would exhibit a much broader range. The results are in the same order of magnitude as the previous estimate based on the same approach and the data for this and other geologically different catchments (6.1–18.6 tC km^{-2} yr^{-1})[5], and as the values assessed by riverine rhenium in two tributaries in this catchment (11–22 tC km^{-2} yr^{-1})[60]. The oxidative flux of OC_{petro} is also comparable with the CO_2 emission of 27 tC km^{-2} yr^{-1} derived from pyrite-induced carbonate weathering in the headwater of the catchment, surpasses the drawdown flux (<10% of pyrite-induced emission) by silicate weathering[61], and rivals the maximum amount

of CO_2 that could be sequestered through the burial of terrestrial biospheric OC for the Beinan catchment (74 ± 22 tC km^{-2} yr^{-1})[18].

For other catchments with rapid erosion rates, the OC_{petro} oxidation fluxes of the Southern Alps in New Zealand and the Swiss pre-Alps are 14–30 tC km^{-2} yr^{-1} [62] and 3.6–5.7 tC km^{-2} yr^{-1} [63], respectively. On the contrary, where erosion rates are low, the OC_{petro} oxidation fluxes are considerably lower (~0.18 tC km^{-2} yr^{-1} for a subcatchment in the Amazon River[6] and up to 1 tC km^{-2} yr^{-1} for Mackenzie River[8]). More specifically, the OC_{petro} oxidation in large river systems proceeds in multiple compartments along the transit. Using the Amazon catchment as an example[14], the flux of OC_{petro} oxidation for the floodplain constitutes 40% of the overall oxidative flux and is only slightly less than that from the mountainous region (46%; $11.2^{4.5}_{-2.8}$ tC km^{-2} yr^{-1}). While the oxidation flux of OC_{petro} in mountainous regions from both large and small river systems are comparable, the lack of broad riparian zone in small river systems impedes longer storage and further oxidation. Overall, our estimation in the Beinan catchment is at the high end for watersheds in active orogens, yet the OC_{petro} oxidation flux for the submarine compartment is not incorporated. Conservative estimation for such submarine component could yield a flux of 0.5 ktC yr^{-1} assuming that 1% of OC_{petro} exported to the ocean (sediment yield = 20 Mt yr^{-1}; TOC_{petro} = 0.27%) is susceptible to microbial degradation (Supplementary Discussion 2). The actual oxidation fraction of the submarine OC_{petro} is warranted to approximate the CO_2 production rate on top of the burial of terrestrial OC_{petro}.

Conclusions

Our study demonstrated prominent shifts in Raman maturity between rocks and weathered materials, and between marine sediments distributed along the submarine canyon. The data pattern suggests two stages of OC_{petro} oxidation from the rock source to the distal marine depocenter. The first stage involves the in situ transformation of highly mature OC_{petro} formed by metamorphism to more disordered graphitic carbon in soil-bedrock profiles or talus deposits. The OC_{petro} with a spectrum of maturity is eroded by mass wasting and transported downstream along with the elimination of mica through abrasion and pulverization prior to being deposited in marine environments. Microbial degradation in river channels appears to impose limited effects on the shift in OC_{petro} maturity. As sediment transport is primarily facilitated by storm- or typhoon-triggered events, the OC_{petro} with a variety of maturities is not detected in riverine sediments but occasionally present either in estuarine or nearshore sediments. The second stage of OC_{petro} oxidation occurs by degrading more disordered graphitic carbon along the submarine canyon, thereby enhancing the preservation frequency of high-maturity OC_{petro} as the transport distance from the shoreline increases. Based on isotopic compositions, the OC_{petro} oxidation in the Beinan catchment contributes to a CO_2 flux of 20–35 tC km^{-2} yr^{-1} from slate and schist. The fluxes alone are comparable to those reported for other mountainous catchments, and offset and even exceed the drawdown contributed by silicate weathering and burial of biospheric OC, highlighting the unique role of mountainous catchments in tectonically active, high-standing islands as a hotspot of CO_2 contributor to the global carbon cycle.

Methods

Site background

The Taiwan mountain belt was formed by the northwestward convergence between the Philippine Sea Plate and Eurasian Plate at a rate of 7 cm yr^{-1} [64]. The burial and subsequent uplift exposed metamorphic rocks trending northeast-southwest in accordance with the stress trajectory. The Backbone Range, as the central part of Taiwan mountain, reached the maximum metamorphism at 3–4 Ma, succeeded by the rapid orographic uplift and terrane cooling during the late Pleistocene[27]. The geological unit of the Backbone Range can be roughly divided into a schist belt to the east and a slate belt to the west. The peak metamorphic temperatures of the schist and slate belts have been estimated to be 550–580 °C and around 450 °C by different approaches, respectively[22,23,65].

The Beinan River and its associated catchment were selected for the investigation because of its high erosion rates[42,43]. Like all the other major rivers originating from the eastern flank of the Backbone Range, the Beinan River crosscuts the Hsinkao Formation (slate belt) and Tananao Complex (schist belt), and turns south into the Longitudinal Valley prior to connecting to the eastward submarine Taitung Canyon (Fig. 1). The lithology of Hsinkao Formation in this area includes slate/phyllite with minor meta-sandstone[66] (Fig. 1a). The Tananao Complex consists of black graphitic schist, subordinate non-carbonaceous light-colored mica schist and greenschist, and minor marble and fine-grained meta-sandstone. An ellipsoidal intrusive metagranite body, with a diameter of ~1 km from the aerial perspective, outcrops in contact with black schist and marble in one of the upstream tributaries (DL)[67]. The river length and drainage area are 84 km and 1603 km^2, respectively. With a high erosion rate up to 30 mm yr^{-1} (exhumation rate by 1.5–10 mm yr^{-1}), the Beinan River exports 20–88 Mt yr^{-1} (~$1–5 \times 10^4$ t km^{-2} yr^{-1}) of suspended load to the ocean[42,43,68], constituting one of the largest river sediment sources in Taiwan and exceeding the global average of area normalized sediment yield by two orders of magnitude[69]. Bathymetry reveals that the exported terrestrial sediments are subsequently channeled into the Huatung Basin east of Taiwan via the Taitung Canyon[45]. Talus deposits are prevalent in the upstream region and range up to dozens of meters in thickness depending on the magnitude of landslide. Because of the short residence time prior to being flushed into rivers, sporadic thin layers of soils develop on top of parental rocks (~10 cm) or poorly sorted talus deposits. The residence time of soil is estimated as shown in Discussion.

Sampling and field processing

Four terrestrial sample categories with a total of 51 samples, including river sediments, bank and sandbar sediments intermittently exposed to the atmosphere, weathered materials, and rocks, were collected (Fig. 1a and Table S1 for detailed site characteristics). A total of 24 river sediments, suspended loads and bedloads, were retrieved from the main stem in the mountain front to the river mouth, and from main tributaries in July 2019. Sediments from the riparian zone at CWL04 (#143) and from the sandbar at the estuary (#137, #178 and #179) were sampled in January and August 2020. The former type of sample was collected next to a minor branch distant from the active channel, thereby presumably remaining intact from most hydraulic erosion for a relatively long period. The sandbar represents the outermost border between the land and the ocean, so the sediments would be episodically immersed in or eroded by seawater or river water. For suspended load, a total of 5 L of river water at each site were drained into the container and filtered using the Whatman GF/F glass microfiber membrane on the same day. For bedload, ~350 mL of wet, relatively fine sediments (<coarse sand) were scooped from the river bed with running water and placed in sterile bags. All the samples were kept frozen in the −20 °C freezer until further processing and analysis.

A total of 16 rock samples, including black schist, slate and meta-sandstone, were collected. The majority of black schists were sampled along the main stem with one exception distributed near the contact with the metagranitic body[67] at the upstream of DL tributary (DLKW). Fine-grained meta-sandstones were collected at LD, whereas slates were sampled from the slate belt flanking both sides of the schist belt.

Eleven weathered materials (~100 mL) were collected from thin soil layers overlying bedrocks, talus deposits, or channel deposits. In addition, soil-parental rock duos were collected at WL (#147–148 and #150–151). These soils (<10 cm thick) appeared as a mixture of black powders and extremely broken fragments of black schist, and were interlayered with their parental rocks. Among all sampling sites for weathered materials, a series of samples with different degrees of soil development from the same hillslope were collected at WL (#150, #148, #173 and #145 in the order of intensifying degrees of weathering). All weathered materials were stored in the −20 °C freezer until further processing and analysis.

Other than land samples, five sediments from seafloor along the Taitung Canyon levee were collected during four expeditions with *R/V New*

Ocean Researcher 3 (NOR3) leg 0012, *R/V Ocean Researcher 1 (OR1)* legs 0960 and 0967, and French *R/V Marion Dufresne (MD)* leg 214 (the EAGER cruise). While the surface sediment at site NOR3-0012-NOR3-1 was retrieved by the Shipek grabber, the rest of sediment samples were acquired from the top 0–1 cm of gravity or box cores at sites OR1-0960-C5, OR1-0967-S1 and MD18-3538-BC (Fig. 1b). In addition, suspended sediments were collected from a sediment trap deployed at site NOR3-0012-NOR3-1 in July 2020, and recovered in September 2020. All sediment samples were collected into 50 mL centrifuge tubes and kept frozen in the −20 °C freezer until further processing and analysis.

Sample processing

Rock samples were cleaned with deionized water to remove potential biospheric organics on the surface. All samples were freeze dried or oven dried at 50 °C. While sediment organic compositions and concentrations vary with different size fractions[47,70,71], the study utilized the materials sieved to less than 63 μm (Mesh = 230) to capture representative and comparable spectroscopic and compositional characteristics of OC_{petro}. Because the grain size of suspended loads and marine sediments was rather uniform and generally smaller than 63 μm, no further sieving was applied. Visible organic detritus was handpicked and excluded from further analysis. Rock samples were crushed, ground and sieved to <63 μm. Hand milling using a pestle and mortar was conducted for less than one hour to avoid the generation of disordered spectra by intense grinding[50].

Analyses of Raman spectroscopy

The analysis of Raman spectroscopy followed the method described in Chen, et al.[72]. Raman spectroscopy was directly performed on dried materials by the Renishaw inVia™ Qontor confocal Raman microscope at National Central University, Taiwan. Calibration with silicon standard was performed before every batch of analyses. Raman spectra were acquired with a 514 nm Ar-ion laser at an 1800 l/mm grating and with a Peltier cooled CCD detector. The laser power on particle surface was set at ~1 mW to ensure that samples were not damaged or transformed during spectrum retrieval. Among graphite-related bands[24,28,73], peak G at 1580 cm^{-1} represents a well-crystallized form, corresponding to in-plane E_{2g} vibration mode of aromatic rings. In contrast, defect bands (D1–D4 bands) are present in disordered carbonaceous materials. The D1 band (1350 cm^{-1}) has been attributed to in-plane defects, causing A_{1g} vibration mode. The D2 (1620 cm^{-1}) and D3 (centers at ~1500 cm^{-1}) bands have been assigned as out-of-plane defects or microcrystallites. The D4 band (1150–1250 cm^{-1}) has been assigned as sp^2-sp^3 bonding, C–C and C=C stretching vibration modes of polyene-like structures, or the H:C ratio in aliphatic hydrocarbon chains.

About 30 particles for each sample were measured to encompass the potential heterogeneity. In order to enable representative and comparable spectroscopic measurements between each sample, extremely small particles (<20 μm) were avoided. The scanning range of Raman spectroscopy was 200–2000 cm^{-1}, covering the first-order bands of graphitic carbon (G, D1–D4 bands). All the identified peaks were deconvoluted by the PeakFit™ v4.06 (SPSS Inc.). The spectra with asymmetric composite D band were fitted into five bands (G, D1–4 bands)[74], whereas the rest of the spectra were deconvoluted into four bands (G, D1–3 bands)[75]. The fitting was manually conducted and iterated until the results converged. The peak position of the fitted D3 band was inspected to be always lower than 1550 cm^{-1} while the G band was retained. As the D2 band was mostly fitted, the position of G band was well constrained to be between those of D2 and D3 bands. Finally, the position of fitted G band was not fixed at a constant value but instead deviated from 1580 cm^{-1} for the well crystalline graphite upon the presence of disordered OC_{petro}. The position variation was well correlated with the so-called Raman band separation (the distance between G and D positions; Fig. S6), which has been shown to decrease with maturity[76].

Deconvoluted Raman parameters were utilized to derive the temperatures following the thermometers described in Beyssac et al.[75] and in Lahfid et al.[74]:

$$T = -445 \times R2 + 641 (330 - 650\ ^{\circ}C) \quad (2)$$

$$T = (RA2 - 0.27)/0.0045 (200 - 320\ ^{\circ}C) \quad (3)$$

where R2 represents the area ratio of D1/(G + D1 + D2) for the temperature range 330–650 °C[75] and RA2 corresponds to the area ratio of (D1 + D4)/(G + D2 + D3) for the temperature range of 200–320 °C[74]. All samples were classified into four groups based on the calculated temperature and total width following the approach described in Sparkes et al.[13]: the Disordered, Intermediate Grade, Mildly Graphitized, and Highly Graphitized OC_{petro} in the order of increasing degrees of graphitization. Spectral signals for minerals in contact with the measured OC_{petro} were also acquired to identify the mineral-OC_{petro} relationships.

Categorization of mineral-OC_{petro} relationships

Due to the small fractions (<1%) of the Highly Graphitized and Disordered OC_{petro} and the scarcity of DLKW-like schists, the OC_{petro} in these two graphitized grades were excluded from statistical analysis. The analysis first proceeded by categorizing OC_{petro} into two groups (Fig. S7). The first one was the attached category, which corresponded to the direct mineral-OC_{petro} association with minerals identifiable by current instrumentation setting. Two potential occurrences were assigned to this category: (1) The target OC_{petro} particle was surrounded by or covered with minerals. For most analyzed spots, the identified minerals were transparent. Even if the mineral overlayed completely on OC_{petro} particle, the Raman spectra for both mineral and OC_{petro} could still be acquired. (2) The target OC_{petro} particle was present without any clear, visible association with minerals. However, the Raman spectra of mineral in addition to OC_{petro} could be acquired. For this occurrence, it was suspected that the mineral was too small to be microscopically visible but detectable by the laser beam with a size of ~1 μm. Therefore, the mineral-OC_{petro} signal acquired from the same laser spot was interpreted as the mineral attached with OC_{petro}. If no signal or signals other than minerals were detected, the OC_{petro} was classified as non-attached category. Three potential occurrences of OC_{petro} were classified into this category: (1) The target OC_{petro} was a free particle. (2) The target OC_{petro} was underlain by minerals. Because OC_{petro} was microscopically and spectroscopically opaque, the underlain mineral phase could not be resolved. (3) The target OC_{petro} was microscopically attached with materials unidentifiable under current instrument setting. These materials might include minerals with indiscernible weak Raman signals and organic materials (e.g., biofilm) as inferred by the brownish appearance of OC_{petro} and/or high spectral background. As soils and sediments are commonly enriched with organic matter, organics-induced fluorescence may generate a high background that can impede the identification of specific organic compounds and organics-incorporated clay minerals[77,78].

Additionally, while the clay fraction (<2 μm) exported from the Beinan River to offshore sediments has been reported to comprise 58% of illite, 35% of chlorite, 5% of smectite, and 2% of kaolinite[46], their summed fraction is supposed to be a small fraction considering the median grain size of 24.9 μm at the river mouth[79]. The diluted fraction combined with the small size of clay rendered the detection of OC_{petro}-clay association (only particles with a size between 20 and 60 μm were measured in this study) challenging.

Overall, the four most prevalent minerals identified in this study included three common rock-forming minerals (quartz, mica, feldspar) and a widely distributed accessory mineral (rutile) in metamorphic rocks. Clay minerals that have been reported as an efficient agent for the protection of organic matter[59,80] were not found because of the potential interference of high spectral background, diluted fraction, and small size that was excluded from the microscopic screening.

The attached group was further categorized into specific mineral types with respect to OC_{petro} maturity. These minerals were categorized as individual mineral groups to increase the count base of individual minerals and to accommodate the limit of the resolving power for Raman spectroscopy.

For example, chalcedony and sericite were grouped with quartz and muscovite (white mica) in Raman spectra, respectively. On the other hand, the resembling spectral characteristics between feldspar group and laumontite (zeolite group) could have resulted in false identification of mineral groups. Multiple minerals attached to OC_{petro} was commonly observed. The counts of minerals were normalized to the total amounts of the analyzed OC_{petro} in each sample (Fig. 4). While the counts of analyzed mineral-OC_{petro} pair relationships for weathered materials, suspended loads and marine sediments are not particularly high (Fig. S7), the interpretation and comparison of mineral abundances for associated OC_{petro} between different material compartments should be cautious.

Analyses of isotopic compositions

About 0.5 g of each sample aliquot was mixed with 5 mL of 2 N HCl thoroughly in a centrifuge tube using a vortex mixer to digest carbonate minerals. The mixture was left to react (at least overnight) at room temperature until bubbling ceased. Samples were centrifuged at 5000 rpm for 5 minutes to remove the acid solution. If vigorous bubbling was observed during the reaction, additional 1–2 mL of 2 N HCl was added again to ensure complete elimination of carbonates. Regardless of acid digestion for one or two times, samples were washed with 8 mL of deionized water for 4–5 times until the pH of solutions returned to neutral. Suspended loads with limited sample volume that could not be scraped from the filter were processed by immersing the filter in the acid solution for several hours until bubbling ceased and washing it with deionized water multiple times. After carbonates removal, all samples were dried at 50 °C. Samples in centrifuge tubes were further ground gently to reduce particle aggregation and avoid potential geochemical heterogeneity. Although acid-soluble OC (e.g., fulvic acids) could be lost during acid leaching, the loss of organic matter during acid leaching and washing has been reported to be only 1.1–4.0% for soils, algae, and sediments[81]. Furthermore, the differences in $\delta^{13}C$ and Fm values after pretreatment have been reported to be <0.6‰[82] and between 0.0006 and 0.1457[83], respectively. Therefore, the potential loss of leachable organic acids and its effect on isotopic composition were assumed to be small, and no further quantitative assessment was performed.

TOC and TN concentrations were determined by an elemental analyzer (Elementar vario MICRO cube EA). Carbon isotopic compositions of TOC and some TOC concentrations for samples with limited volume were determined using an isotope ratio mass spectrometer (Thermo Finnigan Delta V IRMS) coupled to an elemental analyzer (Thermo Flash EA). All the isotopic compositions were reported using δ notation (in permil, ‰; $\delta^{13}C = [(^{13}C/^{12}C)_{sample}/(^{13}C/^{12}C)_{standard} - 1] \times 1000$) with respect to Vienna Pee Dee Bee Belemnite with an uncertainty of ±0.2‰. Eight samples from weathered materials were selected for radiocarbon analyses at Beta Analytic. All the ^{14}C results were expressed as Fraction modern carbon (Fm = the fraction of the normalized ^{14}C activity of the sample relative to the standard).

Data availability

The source data used to generate the charts and raw Raman data can be found in Supplementary Data. Both Supplementary Information and Data have been deposited in Zenodo (https://doi.org/10.5281/zenodo.13627547). Lithology data were obtained from the Geological Survey and Mining Management Agency, MOEA. The DEM, catchment and shoreline data were sourced from Taiwan's open government data platform. The bathymetry data were acquired from the Ocean Data Bank, National Science and Technology Council, Taiwan.

Received: 5 May 2024; Accepted: 9 January 2025;
Published online: 22 January 2025

References

1. Torres, M. A., West, A. J. & Li, G. Sulphide oxidation and carbonate dissolution as a source of CO2 over geological timescales. *Nature* **507**, 346–349 (2014).
2. Gaillardet, J., Dupré, B., Louvat, P. & Allegre, C. Global silicate weathering and CO2 consumption rates deduced from the chemistry of large rivers. *Chem. Geol.* **159**, 3–30 (1999).
3. Spence, J. & Telmer, K. The role of sulfur in chemical weathering and atmospheric CO2 fluxes: evidence from major ions, δ13CDIC, and δ34SSO4 in rivers of the Canadian Cordillera. *Geochim. Cosmochim. Acta* **69**, 5441–5458 (2005).
4. Blattmann, T. M., Letsch, D. & Eglinton, T. I. On the geological and scientific legacy of petrogenic organic carbon. *Am. J. Sci.* **318**, 861–881 (2018).
5. Hemingway, J. D. et al. Microbial oxidation of lithospheric organic carbon in rapidly eroding tropical mountain soils. *Science* **360**, 209–212 (2018).
6. Bouchez, J. et al. Oxidation of petrogenic organic carbon in the Amazon floodplain as a source of atmospheric CO2. *Geology* **38**, 255–258 (2010).
7. Galy, V., Beyssac, O., France-Lanord, C. & Eglinton, T. Recycling of graphite during Himalayan erosion: a geological stabilization of carbon in the crust. *Science* **322**, 943–945 (2008).
8. Horan, K. et al. Carbon dioxide emissions by rock organic carbon oxidation and the net geochemical carbon budget of the Mackenzie River Basin. *Am. J. Sci.* **319**, 473–499 (2019).
9. Ogrič, M. et al. Low rates of rock organic carbon oxidation and anthropogenic cycling of rhenium in a slowly denuding landscape. *Earth Surf. Process. Landf.* **48**, 1202–1218 (2023).
10. Hilton, R. G. & West, A. J. Mountains, erosion and the carbon cycle. *Nat. Rev. Earth Environ.* **1**, 284–299 (2020).
11. Zondervan, J. R. et al. Rock organic carbon oxidation CO2 release offsets silicate weathering sink. *Nature*. https://doi.org/10.1038/s41586-023-06581-9 (2023).
12. Burdige, D. J. Burial of terrestrial organic matter in marine sediments: a re-assessment. *Glob. Biogeochem. Cycles* **19**, https://doi.org/10.1029/2004GB002368 (2005).
13. Sparkes, R. B., Hovius, N., Galy, A. & Liu, J. T. Survival of graphitized petrogenic organic carbon through multiple erosional cycles. *Earth Planet. Sci. Lett.* **531**, 115992 (2020).
14. Dellinger, M. et al. High rates of rock organic carbon oxidation sustained as Andean sediment transits the Amazon foreland-floodplain. *Proc. Natl Acad. Sci.* **120**, e2306343120 (2023).
15. Repasch, M. et al. Fluvial organic carbon cycling regulated by sediment transit time and mineral protection. *Nat. Geosci.* **14**, 842–848 (2021).
16. Leithold, E. L., Blair, N. E. & Wegmann, K. W. Source-to-sink sedimentary systems and global carbon burial: a river runs through it. *Earth Sci. Rev.* **153**, 30–42 (2016).
17. Kao, S. J. et al. Preservation of terrestrial organic carbon in marine sediments offshore Taiwan: mountain building and atmospheric carbon dioxide sequestration. *Earth Surf. Dyn.* **2**, 127–139 (2014).
18. Hilton, R. G. et al. Climatic and geomorphic controls on the erosion of terrestrial biomass from subtropical mountain forest. *Glob. Biogeochem. Cycles* **26**, 1–12 (2012).
19. Clark, K. E. et al. New views on "old" carbon in the Amazon River: insight from the source of organic carbon eroded from the Peruvian Andes. *Geochem. Geophys. Geosyst.* **14**, 1644–1659 (2013).
20. Leithold, E. L., Blair, N. E. & Perkey, D. W. Geomorphologic controls on the age of particulate organic carbon from small mountainous and upland rivers. *Glob. Biogeochem. Cycles* **20**, https://doi.org/10.1029/2005GB002677 (2006).
21. Larsen, I. J. et al. Rapid soil production and weathering in the Southern Alps, New Zealand. *Science* **343**, 637–640 (2014).
22. Beyssac, O. et al. Late Cenozoic metamorphic evolution and exhumation of Taiwan. *Tectonics* **26**, https://doi.org/10.1029/2006TC002064 (2007).

23. Yui, T. F. Isotopic composition of carbonaceous material in metamorphic rocks from the mountain belt of Taiwan. *Int. Geol. Rev.* **47**, 310–325 (2005).
24. Schito, A., Muirhead, D. K. & Parnell, J. Towards a kerogen-to-graphite kinetic model by means of Raman spectroscopy. *Earth Sci. Rev.* **237**, 104292 (2023).
25. Schito, A., Romano, C., Corrado, S., Grigo, D. & Poe, B. Diagenetic thermal evolution of organic matter by Raman spectroscopy. *Org. Geochem.* **106**, 57–67 (2017).
26. Tang, C.-H., Hsu, Y.-J., Barbot, S., Moore, J. D. P. & Chang, W.-L. Lower-crustal rheology and thermal gradient in the Taiwan orogenic belt illuminated by the 1999 Chi-Chi earthquake. *Sci. Adv.* **5**, eaav3287 (2019).
27. Chen, C.-T., Lo, C.-H., Wang, P.-L. & Lin, L.-H. Extensional mountain building along convergent plate boundary: insights from the active Taiwan mountain belt. *Geology* **50**, 1245–1249 (2022).
28. Sadezky, A., Muckenhuber, H., Grothe, H., Niessner, R. & Pöschl, U. Raman microspectroscopy of soot and related carbonaceous materials: spectral analysis and structural information. *Carbon* **43**, 1731–1742 (2005).
29. Ivleva, N., McKeon, U., Niessner, R. & Pöschl, U. Raman microspectroscopic analysis of size-resolved atmospheric aerosol particle samples collected with an ELPI: soot, humic-like substances, and inorganic compounds. *Aerosol Sci. Technol.* **41**, 655–671 (2007).
30. Morales, C. et al. In-situ study of the carbon gasification reaction of highly oriented pyrolytic graphite promoted by cobalt oxides and the novel nanostructures appeared after reaction. *Carbon* **158**, 588–597 (2020).
31. Nair, S. S., Saha, T., Dey, P. & Bhadra, S. Thermal oxidation of graphite as the first step for graphene preparation: effect of heating temperature and time. *J. Mater. Sci.* **56**, 3675–3691 (2021).
32. Contescu, C. I. et al. Practical aspects for characterizing air oxidation of graphite. *J. Nucl. Mater.* **381**, 15–24 (2008).
33. Petsch, S. T., Eglinton, T. I. & Edwards, K. J. 14C-dead living biomass: evidence for microbial assimilation of ancient organic carbon during shale weathering. *Science* **292**, 1127–1131 (2001).
34. Chen, R. et al. Soil C and N availability determine the priming effect: microbial N mining and stoichiometric decomposition theories. *Glob. Change Biol.* **20**, 2356–2367 (2014).
35. Shahbaz, M. et al. Microbial decomposition of soil organic matter is mediated by quality and quantity of crop residues: mechanisms and thresholds. *Biol. Fertil. Soils* **53**, 287–301 (2017).
36. Bernard, L. et al. Advancing the mechanistic understanding of the priming effect on soil organic matter mineralisation. *Funct. Ecol.* **36**, 1355–1377 (2022).
37. Banc, C. et al. pH control on organic and organo-mineral colloids carrying major and trace elements in leachates of wetland sludge deposits. *Chem. Eng. J.* **471**, 144244 (2023).
38. Keiluweit, M. et al. Mineral protection of soil carbon counteracted by root exudates. *Nat. Clim. Change* **5**, 588–595 (2015).
39. Fang, Q. et al. Mineral weathering is linked to microbial priming in the critical zone. *Nat. Commun.* **14**, 345 (2023).
40. Amundson, R. In: *Treatise on Geochemistry* (Second Edition) (eds. Heinrich D. H. & Karl K. T.) 1–26 (Elsevier, 2014).
41. Lebedeva, M. I. & Brantley, S. L. Weathering and erosion of fractured bedrock systems. *Earth Surf. Process. Landf.* **42**, 2090–2108 (2017).
42. Chen, C. Y., Willett, S. D., Christl, M. & Shyu, J. B. H. Drainage basin dynamics during the transition from early to mature orogeny in Southern Taiwan. *Earth Planet. Sci. Lett.* **562**, 116874 (2021).
43. Dadson, S. J. et al. Links between erosion, runoff variability and seismicity in the Taiwan orogen. *Nature* **426**, 648–651 (2003).
44. Hilton, R. G., Galy, A., Hovius, N., Horng, M.-J. & Chen, H. The isotopic composition of particulate organic carbon in mountain rivers of Taiwan. *Geochim. Cosmochim. Acta* **74**, 3164–3181 (2010).
45. Lehu, R. et al. Deep-sea sedimentation offshore eastern Taiwan: facies and processes characterization. *Mar. Geol.* **369**, 1–18 (2015).
46. Nayak, K. et al. Clay-mineral distribution in recent deep-sea sediments around Taiwan: implications for sediment dispersal processes. *Tectonophysics* **814**, 228974 (2021).
47. Tesi, T., Semiletov, I., Dudarev, O., Andersson, A. & Gustafsson, Ö. Matrix association effects on hydrodynamic sorting and degradation of terrestrial organic matter during cross-shelf transport in the Laptev and East Siberian shelf seas. *J. Geophys. Res.: Biogeosci.* **121**, 731–752 (2016).
48. Arnarson, T. S. & Keil, R. G. Changes in organic matter–mineral interactions for marine sediments with varying oxygen exposure times. *Geochim. Cosmochim. Acta* **71**, 3545–3556 (2007).
49. Tanabe, T. Radiation damage of graphite - degradation of material parameters and defect structures. *Phys. Scr.* **1996**, 7 (1996).
50. Xing, T. et al. Disorder in ball-milled graphite revealed by Raman spectroscopy. *Carbon* **57**, 515–519 (2013).
51. Welham, N. J. & Williams, J. S. Extended milling of graphite and activated carbon. *Carbon* **36**, 1309–1315 (1998).
52. Henschke, B., Schubert, H., Blöcker, J., Atamny, F. & Schlögl, R. Mechanistic aspects of the reaction between carbon and oxygen. *Thermochim. Acta* **234**, 53–83 (1994).
53. Blair, N. E. & Aller, R. C. The fate of terrestrial organic carbon in the marine environment. *Annu. Rev. Mar. Sci.* **4**, 401–423 (2012).
54. Hsu, H.-H., Liu, C.-S., Chen, T.-T. & Hung, H.-T. Stratigraphic framework and sediment wave fields associated with canyon-levee systems in the Huatung Basin offshore Taiwan Orogen. *Mar. Geol.* **433**, 106408 (2021).
55. Morton, A. C. & Hallsworth, C. R. Processes controlling the composition of heavy mineral assemblages in sandstones. *Sediment. Geol.* **124**, 3–29 (1999).
56. Palandri, J. L. & Kharaka, Y. K. A compilation of rate parameters of water-mineral interaction kinetics for application to geochemical modeling. Report No. 2004–1068 (2004).
57. Heřmanská, M., Voigt, M. J., Marieni, C., Declercq, J. & Oelkers, E. H. A comprehensive and internally consistent mineral dissolution rate database: part I: primary silicate minerals and glasses. *Chem. Geol.* **597**, 120807 (2022).
58. Heřmanská, M., Voigt, M. J., Marieni, C., Declercq, J. & Oelkers, E. H. A comprehensive and consistent mineral dissolution rate database: part II: secondary silicate minerals. *Chem. Geol.* **636**, 121632 (2023).
59. Keil, R. G. & Mayer, L. M. In: *Treatise on Geochemistry (2nd Edition)* Vol. 12 (eds Heinrich D. H., & Karl K. T.) 337–359 (Elsevier, 2014).
60. Hilton, R. G., Gaillardet, J., Calmels, D. & Birck, J.-L. Geological respiration of a mountain belt revealed by the trace element rhenium. *Earth Planet. Sci. Lett.* **403**, 27–36 (2014).
61. Wang, P.-L. et al. Microbial communities modulate chemical weathering and carbon dioxide cycling in an active orogen in Taiwan. *Commun. Earth Environ.* **5**, 174 (2024).
62. Horan, K. et al. Mountain glaciation drives rapid oxidation of rock-bound organic carbon. *Sci. Adv.* **3**, e1701107 (2017).
63. Hilton, R. G. et al. Concentration-discharge relationships of dissolved rhenium in Alpine catchments reveal its use as a tracer of oxidative weathering. *Water Resour. Res.* **57**, e2021WR029844 (2021).
64. Teng, L. S. Geotectonic evolution of late Cenozoic arc-continent collision in Taiwan. *Tectonophysics* **183**, 57–76 (1990).
65. Baziotis, I., Tsai, C. H., Ernst, W. G., Jahn, B. M. & Iizuka, Y. New P–T constraints on the Tamayen glaucophane-bearing rocks, eastern Taiwan: Perple_X modelling results and geodynamic implications. *J. Metamorph. Geol.* **35**, 35–54 (2017).
66. Stanley, R. S., RS, S., LB, H., HC, C. & HN, H. In: Memoir of the Geological Society of China. vol. 4, 443–473 (1981).
67. Yui, T. F. et al. Subduction-related 200 Ma Talun metagranite, SE Taiwan: an age constraint for Palaeo-Pacific plate subduction

beneath South China block during the Mesozoic. *Int. Geol. Rev.* **59**, 333–346 (2017).
68. Kao, S. J. & Milliman, J. D. Water and sediment discharge from small mountainous rivers, Taiwan: the roles of lithology, episodic events, and human activities. *J. Geol.* **116**, 431–448 (2008).
69. Milliman, J. D. & Farnsworth, K. L. River discharge to the coastal ocean: a global synthesis (Cambridge University Press, 2011).
70. Bao, R., Blattmann, T. M., McIntyre, C., Zhao, M. & Eglinton, T. I. Relationships between grain size and organic carbon 14C heterogeneity in continental margin sediments. *Earth Planet. Sci. Lett.* **505**, 76–85 (2019).
71. Yu, M. et al. Molecular isotopic insights into hydrodynamic controls on fluvial suspended particulate organic matter transport. *Geochim. Cosmochim. Acta* **262**, 78–91 (2019).
72. Chen, C.-T. et al. Thermal history of the northern taiwanese slate belt and implications for wedge growth during the neogene arc-continent collision. *Tectonics* **38**, 3335–3350 (2019).
73. Beyssac, O. et al. On the characterization of disordered and heterogeneous carbonaceous materials by Raman spectroscopy. *Spectrochim. Acta Part A: Mol. Biomol. Spectrosc.* **59**, 2267–2276 (2003).
74. Lahfid, A. et al. Evolution of the Raman spectrum of carbonaceous material in low-grade metasediments of the Glarus Alps (Switzerland). *Terra Nova* **22**, 354–360 (2010).
75. Beyssac, O., Goffé, B., Chopin, C. & Rouzaud, J. Raman spectra of carbonaceous material in metasediments: a new geothermometer. *J Metamorp. Geol.* **20**, 859–871 (2002).
76. Henry, D. G., Jarvis, I., Gillmore, G. & Stephenson, M. Raman spectroscopy as a tool to determine the thermal maturity of organic matter: application to sedimentary, metamorphic and structural geology. *Earth Sci. Rev.* **198**, 102936 (2019).
77. Wang, A., Freeman, J. J. & Jolliff, B. L. Understanding the Raman spectral features of phyllosilicates. *J. Raman Spectrosc.* **46**, 829–845 (2015).
78. Ess, M. N. et al. In situ Raman microspectroscopic analysis of soot samples with different organic carbon content: structural changes during heating. *Carbon* **105**, 572–585 (2016).
79. Lin, B. et al. Island-wide variation in provenance of riverine sedimentary organic carbon: a case study from Taiwan. *Earth Planet. Sci. Lett.* **539**, 116238 (2020).
80. Barré, P., Fernandez-Ugalde, O., Virto, I., Velde, B. & Chenu, C. Impact of phyllosilicate mineralogy on organic carbon stabilization in soils: incomplete knowledge and exciting prospects. *Geoderma* **235**, 382–395 (2014).
81. Brodie, C. R. et al. Evidence for bias in C and N concentrations and δ13C composition of terrestrial and aquatic organic materials due to pre-analysis acid preparation methods. *Chem. Geol.* **282**, 67–83 (2011).
82. Kim, M.-S. et al. Effects of HCl pretreatment, drying, and storage on the stable isotope ratios of soil and sediment samples. *Rapid Commun. Mass Spectrom.* **30**, 1567–1575 (2016).
83. Bao, R., McNichol, A. P., Hemingway, J. D., Lardie Gaylord, M. C. & Eglinton, T. I. Influence of different acid treatments on the radiocarbon content spectrum of sedimentary organic matter determined by RPO/accelerator mass spectrometry. *Radiocarbon* **61**, 395–413 (2019).
84. Lamb, A. L., Wilson, G. P. & Leng, M. J. A review of coastal palaeoclimate and relative sea-level reconstructions using δ13C and C/N ratios in organic material. *Earth Sci. Rev.* **75**, 29–57 (2006).

Acknowledgements

This research was financially supported by the Taiwan Ministry of Education and National Science and Technology Council (113-2116-M-002-018-MY3 to LHL and 113-2116-M-002-027- to PLW). None of the samples were retrieved from restricted areas. We thank Ya-Fang Cheng, I-Feng Wu, Hsin-No Kuo, Tzu-Jung Cheng, Nai-Chen Chen, Yueh-Ting Lin, and Jui-Ming Chang for the help with sample collection, and Ya-Chi Su for the assistance of the analysis of Raman spectroscopy. We are grateful to the captain and crew of the *R/V Ocean Researcher 1, R/V New Ocean Researcher 3*, and French *R/V Marion Dufresne* for their help with submarine sample retrieval. We also appreciate the invaluable comments provided by the editors and reviewers.

Author contributions

W.Y.L.: conceptualization, methodology, formal analysis, investigation, writing–original draft. C.T.C., Y.H.L., and C.C.S.: resources, writing–review & editing. P.L.W. and L.H.L.: conceptualization, methodology, resources, writing–review & editing, funding acquisition.

Competing interests

The authors declare no competing interests.

Additional information

Supplementary information The online version contains supplementary material available at https://doi.org/10.1038/s43247-025-02015-8.

Correspondence and requests for materials should be addressed to Pei-Ling Wang or Li-Hung Lin.

Peer review information *Communications Earth & Environment* thanks Robert Sparkes and the other, anonymous, reviewer(s) for their contribution to the peer review of this work. Primary Handling Editors: Joshua Dean and Carolina Ortiz Guerrero. A peer review file is available.

Reprints and permissions information is available at http://www.nature.com/reprints

Publisher's note Springer Nature remains neutral with regard to jurisdictional claims in published maps and institutional affiliations.

Open Access This article is licensed under a Creative Commons Attribution-NonCommercial-NoDerivatives 4.0 International License, which permits any non-commercial use, sharing, distribution and reproduction in any medium or format, as long as you give appropriate credit to the original author(s) and the source, provide a link to the Creative Commons licence, and indicate if you modified the licensed material. You do not have permission under this licence to share adapted material derived from this article or parts of it. The images or other third party material in this article are included in the article's Creative Commons licence, unless indicated otherwise in a credit line to the material. If material is not included in the article's Creative Commons licence and your intended use is not permitted by statutory regulation or exceeds the permitted use, you will need to obtain permission directly from the copyright holder. To view a copy of this licence, visit http://creativecommons.org/licenses/by-nc-nd/4.0/.

© The Author(s) 2025